

ARTICLE

Open Access

# Single-particle tracking of the formation of a pseudoequilibrium state prior to charged microgel cluster formation at interfaces

Wuguo Bi<sup>1</sup> and Edwin K. L. Yeow<sup>2</sup>

## Abstract

The correlation between micron-sized particles and their self-assembly at fluid interfaces is important in several applications, including the stabilization of Pickering emulsions and creation of colloidosomes. In this study, through real-time visualization of the diffusion of microgel particles at the air–water interface of an aqueous pendant drop, the formation of a pseudoequilibrium state is observed prior to cluster formation. It is shown here that at the microscopic level, a pendant drop surface has nonuniform principal curvatures and exhibits positive deviatoric curvature ( $+\Delta c$ ) gradients. The  $+\Delta c$  gradients confer superdiffusive motion to single ionic microgel particles and are responsible for bringing particles that are initially far apart to common sites on the interface with high curvatures. Prior to two-particle cluster formation, the balance between pairwise repulsion, capillary attraction and  $+\Delta c$ -induced energy that pushes the pair of particles to a high curvature creates a pseudoequilibrium state where the interparticle distance remains relatively invariant for a long period of time. This observation is also noted during higher-order cluster formation. Thereafter, a sufficiently strong long-range attraction potential is activated to facilitate cluster formation. Real-time tracking of the evolution of cluster formation provides useful insights into the interplay between various interactions experienced by ionic microgels.

## Introduction

Without the use of potentially harmful surfactants, micron-sized particles can stabilize emulsions by adsorbing onto their interfaces (i.e., Pickering emulsions)<sup>1</sup>. Due to the soft nature of microgel particles, the interfacial free energy is decreased further when the trapped microgels undergo deformation at the interface<sup>2–5</sup>. This allows microgel particles to adsorb readily and thus act as suitable emulsion stabilizers<sup>6–9</sup>. When dispersed in a good solvent, microgels (e.g., those based on poly(N-isopropylacrylamide) (PNIPAM)) are able to swell due to solvent penetration into the soft particles<sup>10–12</sup>. The presence of a polymer cross-linking gradient results in a hard

core with high cross-linking density and a soft corona of loose cross-linked chains. When PNIPAM microgels are adsorbed at the liquid/liquid interface, they adopt a “fried egg-like” morphology with diameters larger than those in the bulk<sup>5,6,13</sup>. The factors affecting the shape of the stretched microgel at the interface, including solvation of the particle in the two phases, surface activity and internal elasticity, have been extensively studied both experimentally and computationally<sup>14–18</sup>.

To improve the stability of Pickering emulsions, it is necessary to understand the interactions between particles and the factors that drive their self-assembly<sup>16</sup>. Interactions between hard colloidal particles (e.g., electrostatic repulsion and long-range attraction) at interfaces have received a substantial amount of attention despite uncertainties in some of the proposed models<sup>19–34</sup>. In contrast, the effective interactions between microgel particles in bulk solvents become more complex as a result of deformation, compression and interpenetration

Correspondence: Wuguo Bi ([wgbih@hrbeu.edu.cn](mailto:wgbih@hrbeu.edu.cn)) or Edwin K. L. Yeow ([edwinyeow@ntu.edu.sg](mailto:edwinyeow@ntu.edu.sg))

<sup>1</sup>College of Physics and Optoelectronic Engineering, Harbin Engineering University, Harbin 150001, China

<sup>2</sup>Division of Chemistry and Biological Chemistry, School of Physical and Mathematical Sciences, Nanyang Technological University, 21 Nanyang Link, Singapore 636371, Singapore

© The Author(s) 2020



**Open Access** This article is licensed under a Creative Commons Attribution 4.0 International License, which permits use, sharing, adaptation, distribution and reproduction in any medium or format, as long as you give appropriate credit to the original author(s) and the source, provide a link to the Creative Commons license, and indicate if changes were made. The images or other third party material in this article are included in the article's Creative Commons license, unless indicated otherwise in a credit line to the material. If material is not included in the article's Creative Commons license and your intended use is not permitted by statutory regulation or exceeds the permitted use, you will need to obtain permission directly from the copyright holder. To view a copy of this license, visit <http://creativecommons.org/licenses/by/4.0/>.

of soft particles and dangling ends, corona–corona, core–corona, core–core, and microgel–counterion interactions need to be considered<sup>35</sup>. Electrostatic repulsion between charged soft-shell/hard-core nanoparticles at the air–water interface has been shown to be responsible for their long-range ordering at low particle densities<sup>36</sup>. This was further supported by a recent computational modeling study that utilized electrostatic repulsion to understand long-range ordering of charged microgels at interfaces that were separated by distances larger than the particle size<sup>37</sup>. Interestingly, at a high particle density or when two-dimensional particle arrays are compressed, charged microgels at interfaces undergo compression more easily than uncharged ones, indicating that electrostatic repulsion plays only a minor role when particles are packed closely together<sup>38</sup>. Instead, coronas of neighboring microgels are able to interpenetrate and compress such that steric interaction and surface activity involving loose chains at the particle periphery contribute to short-range repulsive interactions<sup>38–42</sup>.

It is known that particles with rough and chemically heterogeneous surfaces or irregular shapes can create contact line undulations that cause perturbations in the surrounding fluid interface. Stamou et al.<sup>24</sup> and Danov et al.<sup>43</sup> have shown that for large separations between spherical particles on a planar interface, capillary attraction due to the quadrupole term is important<sup>44</sup>. On the other hand, when the particles approach each other (i.e., on the order of the particle size), interactions between higher multipole orders come into play and can be repulsive in nature<sup>24,43,44</sup>. As demonstrated by Stebe et al., near field capillary repulsion is apparent between a pair of nonspherical objects with out-of-phase undulations<sup>45,46</sup>. Since soft particles have rough and chemically heterogeneous surfaces and their wetting radii are elongated at interfaces<sup>16</sup>, long-range capillary attraction between neutral microgels adsorbed at planar interfaces has been proposed to be responsible for the formation of aggregates<sup>47–49</sup>.

A commonly invoked mechanism to explain the self-organization of colloidal particles trapped at curved interfaces involves capillary interactions arising from curvature gradients that push the particles to regions of steep curvature<sup>50,51</sup>. In particular, this was nicely demonstrated for colloidal particles that adhered to tense lipid bilayers<sup>52,53</sup>. An area that remains relatively unexplored is the understanding of the evolution of events leading to cluster formation between sparsely distributed ionic microgel particles at a curved liquid interface.

The single-molecule/particle tracking technique is a powerful tool to track the motion of single fluorescent molecules/particles and can be achieved via fluorescence wide-field microscopy (WFM). WFM was previously used to study polymer physics (e.g., crystallization of single

polymeric chains in thin layers)<sup>54</sup>, dynamics of single swarming bacteria<sup>55</sup> and catalysis<sup>56</sup>. WFM has also been utilized to understand, at the bulk level, materials-related phenomena, such as hole nucleation and growth in polymer blend films<sup>57</sup>, the coffee ring effect<sup>58</sup>, and drug-release dynamics from antibiotic carriers to tackle bacterial infection<sup>59</sup>. In this study, WFM demonstrates that at the microscopic level, the air–water interface of an aqueous pendant drop has nonuniform principal curvatures that not only confer superdiffusive motion to single like-charged particles but also transport them closer together at a common area on the interface. The latter is a necessary step that precedes self-assembly. In particular, the interplay between various forces on the evolution of cluster formation starting from particles that are initially far apart (i.e., longer than twice the contact radius) is examined here.

## Materials and methods

### Materials

*N*-Isopropylacrylamide (NIPAM) (97%), *N,N'*-methylenebisacrylamide (BIS) (99%), 2-aminoethyl methacrylate hydrochloride (AEMH) (90%), and potassium peroxydisulfate (KPS) (99%) were purchased from Sigma-Aldrich. Acetic acid (99.8%), sodium carbonate (anhydrous, 99.5%) and sodium bicarbonate (99%) were purchased from Schedelco, Sinopharm Chemical and Chemicon, respectively. ATTO 647N NHS-ester and ATTO 550 NHS-ester dyes were obtained from ATTO-Tec GmbH. All chemicals above were used as received. *N,N*-dimethylformamide (DMF) (HPLC/Spectroscopy grade) was obtained from Tedia and dried by a molecular sieve (4A, Sigma-Aldrich) before use.

### Synthesis of the microgel particles

The microgel particles were synthesized by first mixing NIPAM (3.2 g, 188.52 mM), AEMH (0.06 g, 2.42 mM), and BIS (0.0985 g, 4.26 mM) in DI water (150 mL)<sup>60</sup>. The pH of the mixture was adjusted to 3.3 by the addition of acetic acid. The solution was then refluxed at ~73 °C for 1 h under an argon atmosphere before adding KPS (0.0364 g, 0.90 mM) to initiate the reaction. The reaction was stopped after 6 h and allowed to cool to room temperature. The resulting P(NIPAM-*co*-AEMH) particles were retrieved by centrifugation and washed with DI water. The average radius of the particles was measured using dynamic light scattering (Malvern Zetasizer Nano).

### Determination of the bare charge on the microgel particles and zeta-potential

The bare charge on a microgel particle method was determined using a spectrophotometric method described in ref. <sup>61</sup>. Briefly, a known and excess concentration of ATTO 550 NHS-ester dye (Atto-Tec GmbH, charge of

+1, extinction coefficient at 554 nm is  $1.2 \times 10^5 \text{ M}^{-1} \text{ cm}^{-1}$  in buffer) was prepared, and 100  $\mu\text{L}$  of the solution was added into a carbonate/bicarbonate buffer solution (1 mL, 107 mM, pH = 8.94) containing P(NIPAM-*co*-AEMH) particles (0.5 mL,  $65.6 \pm 9.3 \text{ mg mL}^{-1}$ ). The mixture was stirred for 5 h. After centrifugation (12,000 rpm for 30 min), the amount of free dye in the supernatant was determined using an absorption spectrometer (Cary 100, Varian). By assuming that all the  $-\text{NH}_2$  groups on the particles formed amide bonds with the dye, the number of  $-\text{NH}_2$  was estimated from the concentration of dye molecules attached to the particles (i.e., difference in the concentrations of free dye before and after reaction with the particles). To determine the number of labelled particles retrieved after centrifugation, the particles were first dispersed in DI water (785  $\mu\text{L}$ ). A quantity of 5  $\mu\text{L}$  of the solution was added into 10 mL of DI water, and then 0.20/0.25/0.29  $\mu\text{L}$  of the resulting solution was drop cast onto a clean coverslip. After evaporating the solvent, the image of the area of the coverslip containing the particles was recorded using a confocal laser scanning microscope (Zeiss LSM 800). The number of microgel particles was counted (Supplementary Fig. S1 in Supplementary Information). The number of bound dye molecules and hence the number of  $-\text{NH}_2$  groups per particle were subsequently determined. This was equivalent to the charge  $Z$  of a microgel at pH = 5.33 arising from the  $-\text{NH}_3^+$  groups.

The zeta potential of the microgels was determined by dispersing 10  $\mu\text{L}$  of the microgel solution ( $65.6 \pm 9.3 \text{ mg mL}^{-1}$ ) in 1 mL of DI water (pH = 5.33). The resulting solution was transferred into a potential sample cell (cuvette DTS1070), and the zeta potential was measured at 25 °C using dynamic light scattering (Malvern Zetasizer Nano).

#### Determination of the surface roughness of the microgel particles

To determine the surface roughness of the microgel particles in air, a sample was prepared by drop casting a concentrated solution of the microgel particles ( $65.6 \pm 9.3 \text{ mg mL}^{-1}$ ) onto a clean silicon wafer and drying for 24 h at room temperature. The surface roughness was determined using atomic force microscopy (Bruker, Multimode 8).

#### Dye labeling of the microgel particles

A dilute DMF solution (50  $\mu\text{L}$ ) of ATTO 647N NHS-ester dye (+1 net charge ATTO-TEC GmbH) was prepared before the addition of a carbonate/bicarbonate buffer solution (1 mL, 107 mM, pH = 8.94). P(NIPAM-*co*-AEMH) microgel particles (500  $\mu\text{L}$ ) were subsequently added into the solution and stirred at room temperature for 5 h. The ATTO 647N dye molecules were covalently

bonded to the particles via an amide bond. The dye-labeled colloidal particles were retrieved by centrifugation (12,000 rpm for 15 min) and redispersed in DI water. This step was repeated >10 times to ensure the removal of free dyes. The collected dye-labeled particles were collected and stored at 4 °C before use.

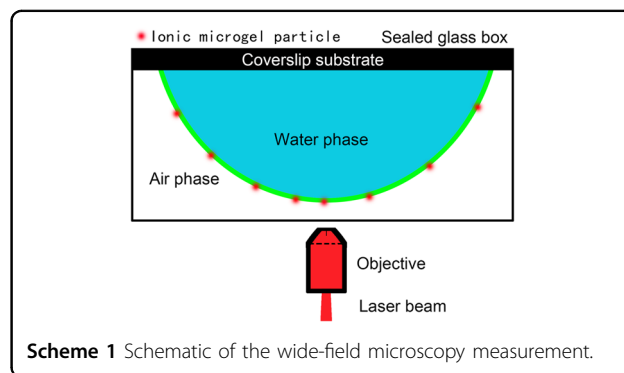
#### Cryo-SEM imaging

A droplet of an aqueous P(NIPAM-*co*-AEMH) microgel suspension (0.5  $\mu\text{L}$ ) was first prepared on the surface of a standard copper holder of a cryo-SEM preparation system (PP3010T, Quorum Technologies Ltd.). The droplet was kept at room temperature for ~3 min before being frozen at  $-190^\circ\text{C}$ . The frozen droplet was then mounted onto a nitrogen gas cooled stage in a chamber followed by the sputtering of gold onto the droplet surface at a 10 mA current for 60 s. Subsequently, the sample was pushed into a chamber on the cryo-SEM (Hitachi SU8010) that was maintained at a high vacuum ( $<5 \times 10^{-7}$  mbar) and low temperature ( $-140^\circ\text{C}$ ) for imaging.

#### Wide-field microscopy

The glass coverslip substrates (20 mm  $\times$  20 mm) were first precleaned by sonication in acetone (HPLC, Tedia) for 10 min followed by sonication in aqueous sodium hydroxide (Scharlau) for 30 min and then sonication in DI water for 10 min. The last step was repeated at least three times. The cleaned coverslips were subsequently rinsed with DI water and dried by blowing argon over the coverslips. The cleaned coverslips were further dried at 80 °C in an oven for more than 1 h.

The aqueous pendant droplet was prepared as follows. A 7  $\mu\text{L}$  aqueous solution containing microgel particles (pH = 5.33) was deposited onto a cleaned coverslip substrate to form an aqueous droplet, which was inverted to obtain the pendant drop, as illustrated in Scheme 1 (see also Supplementary Fig. S2). The sample was placed inside a sealed homemade glass box to minimize evaporation. Subsequently, WFM measurements were performed.



For experiments examining microgels on a planar air–water interface, a polytetrafluoroethylene ring with dimensions of 5 mm (diameter)  $\times$  5 mm (height) was fixed onto a cleaned coverslip, and a 50  $\mu$ L aqueous solution of microgel particles (pH = 5.33) was placed into the ring. Subsequently, a cleaned coverslip was used to cover the top to prevent evaporation of the solution.

The wide-field fluorescence microscopy setup consisted of a microscope (IX 71, Olympus) and a 633 nm HeNe laser source (75 mW, Melles Griot). The excitation light was tuned to be circularly polarized using  $\lambda/4$  and  $\lambda/2$  waveplates and expanded via a beam expander (ThorLabs) before being focused onto the back-focal plane of an air objective lens (20 $\times$ , N.A. = 0.4, Olympus). An excitation filter (Z633/10, Chroma) was used to filter the excitation light. The fluorescence was passed through a dichroic mirror (Z633rdc, Chroma) and an emission filter (HQ645lp, Chroma) and subsequently detected by a highly sensitive CCD camera (CascadeII 512B, Photometrics) after magnification with a 3.3 $\times$  camera lens. The integration time of the CCD camera was 34.6 ms per frame. The trajectories of the microgel particles were obtained according to ref. <sup>62</sup>. The coordinates of the center of the cluster were the average coordinates of the center of each particle forming the cluster. The diffraction-limited spatial resolution was  $\sim$ 791 nm.

#### Confocal fluorescence imaging of the water pendant droplets

The pendant drop in a sealed container was imaged using a confocal laser scanning microscope (Zeiss LSM 800) using a 640 nm diode laser and 20 $\times$  air objective (N.A. = 0.5, Zeiss). The size of the horizontal  $x$ – $y$  plane

imaged was  $512 \times 512$  pixels corresponding to  $639 \times 639 \mu\text{m}^2$ , and a vertical  $z$ -step of 2  $\mu\text{m}$  was used. The coordinates were obtained from Fiji (ImageJ) software.

## Results and discussion

### Microgel particles at the air–water interface

The P(NIPAM-*co*-AEMH) microgel particles used in this study are prepared by copolymerizing and cross-linking NIPAM and AEMH in the presence of BIS and KPS. The average hydrodynamic radius of the particles in DI water (pH = 5.33) is determined by dynamic light scattering to be  $a_w = 0.44 \pm 0.05 \mu\text{m}$ . At this pH, the AEMH monomers dissociate to form positive charges and the zeta-potential is  $+21.0 \pm 0.5 \text{ mV}$ . The bare charge of each microgel particle is  $Z \sim (2.01 \pm 0.20) \times 10^5 e$  and the Debye length  $\kappa^{-1} = 142 \text{ nm}$  (see Text S1). The microgel particles are subsequently conjugated to ATTO 647N dye molecules before being dispersed in DI water. Since the dye carries a net positive charge of +1, the bare charge of the microgel particles after labeling remains unchanged.

A pendant drop of the microgel solution (pH = 5.33) that is supported on a coverslip with a substrate contact radius of  $\sim$ 2.1 mm is placed inside a sealed container to minimize evaporation (Scheme 1). The microgel particle density at the air–water interface is kept low to avoid multibody and third body interactions during the single particle ( $2 \times 10^{-4}$  particles  $\mu\text{m}^{-2}$  area) and particle pair ( $1 \times 10^{-3}$  particles  $\mu\text{m}^{-2}$ ) studies, respectively.

The conformation of the microgel particles trapped at the air–water interface is examined using cryo-SEM. Figure 1a shows the front view of the particles that are imaged from the air side, where the core–corona morphology is observed. The radii of the core and total

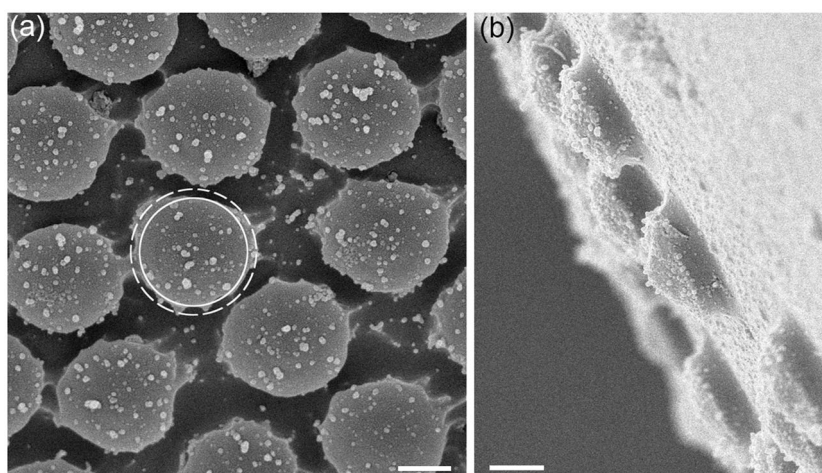
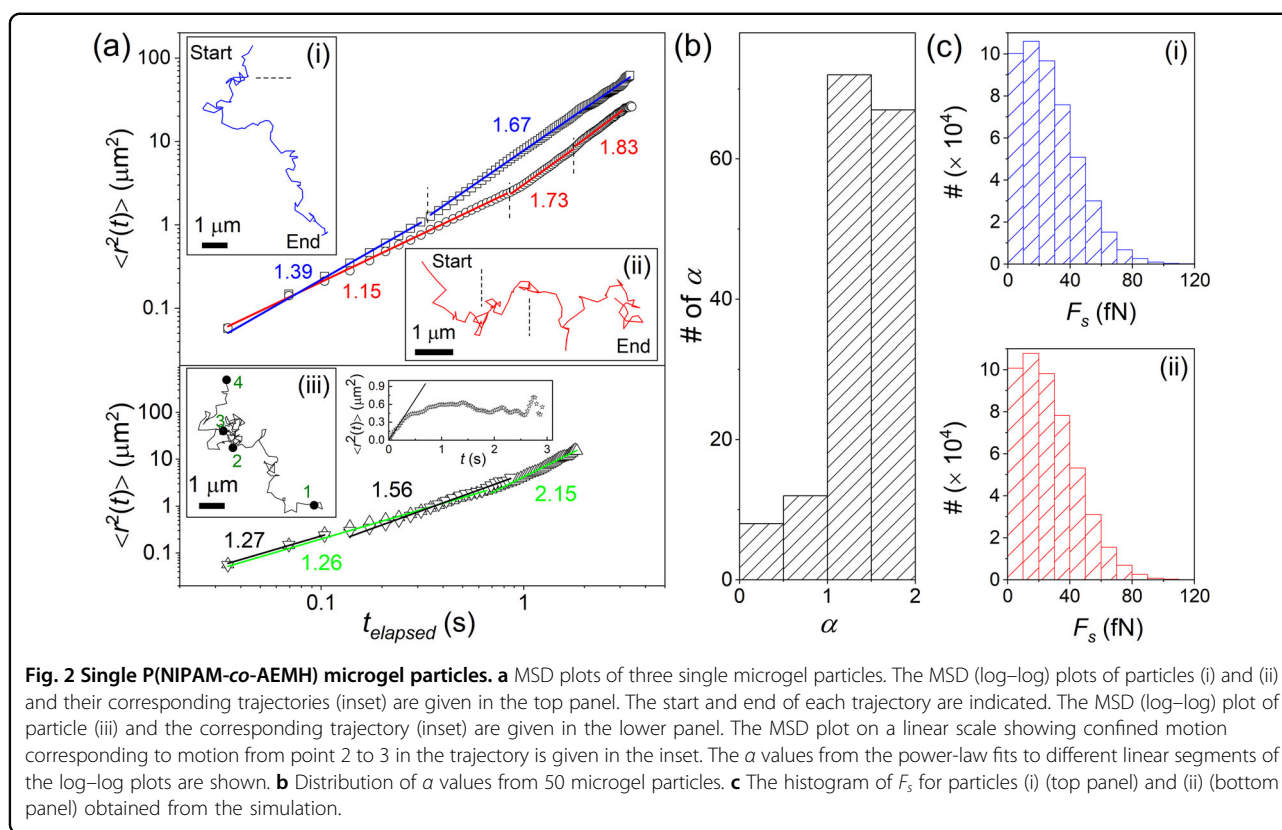


**Fig. 1** Single P(NIPAM-*co*-AEMH) microgel particles trapped at the air–water interface. **a**, **b** The cryo-SEM images of the microgel particles at the air–water interface imaged from the air side. **a** The front view where the core and core–corona of one of the particles are enclosed in a solid circle and dotted circle, respectively. **b** The side view of the particles exposed to air. Residual ice is deposited on the surface of microgels. The scale bars in **(a)** and **(b)** are 500 nm.



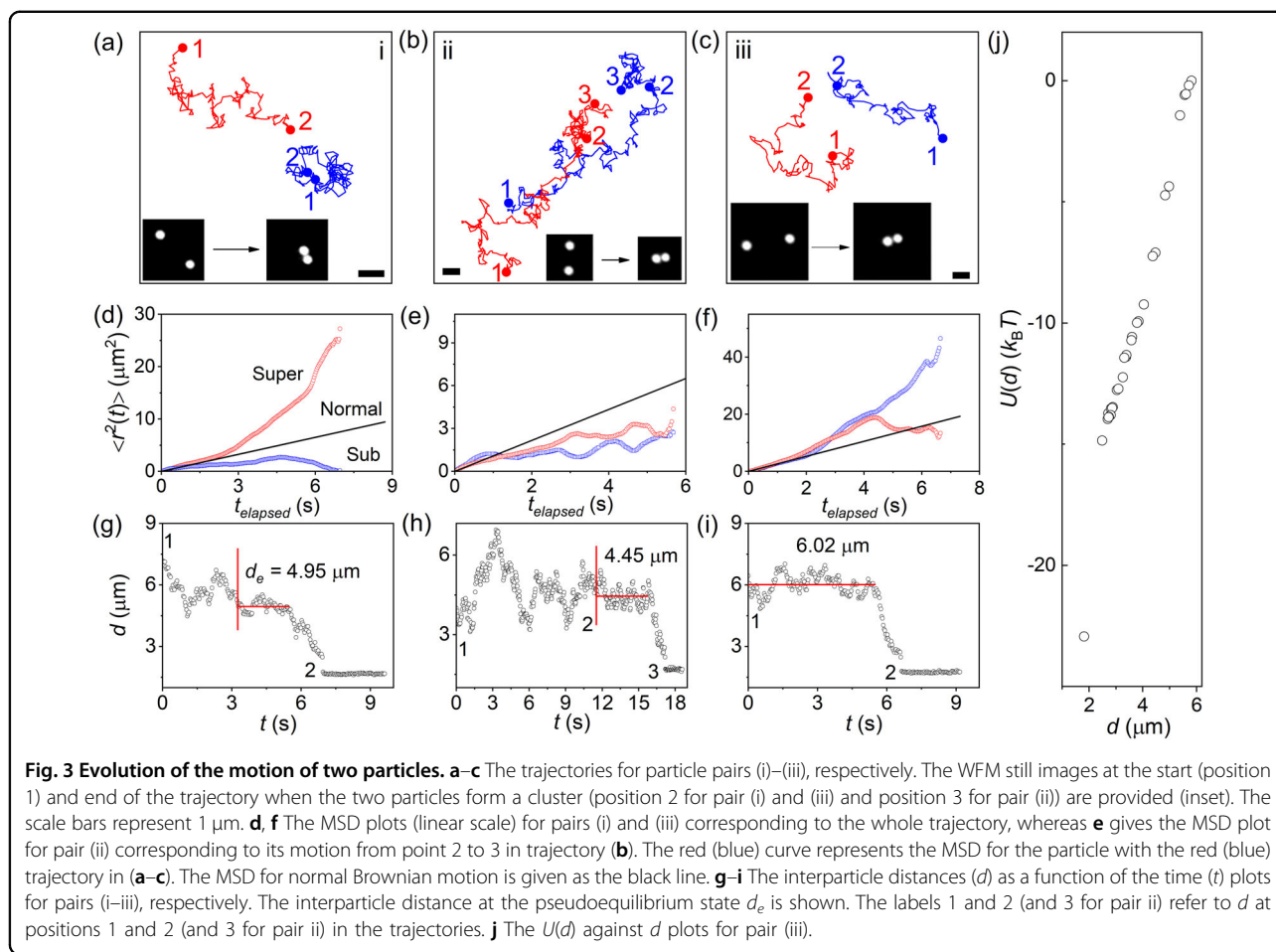
microgel (i.e., core and corona) at the interface are determined to be  $a_c = 0.53 \pm 0.02 \mu\text{m}$  and  $a = 0.63 \pm 0.02 \mu\text{m}$ , respectively. The side view in Fig. 1b clearly shows the microgels adopting a sort of “fried egg-like” morphology, where the particles are stretched at the interface when compared to their spherical shape in bulk solution<sup>5,6,13</sup>. Even if traces of water exist within the air-exposed portion of the microgel, the effect of volumetric expansion upon ice formation (i.e., 9%) does not account for the observed interface stretching, which is instead dependent on the particle surface tension and its elastic and plastic deformation properties (i.e., Young’s modulus and yield stress)<sup>5</sup>. Assuming that the volume of a microgel in bulk solution does not change when trapped at an air–water interface, the particle volume submerged in the water phase is estimated to be  $\sim 25\%$  of its total volume (Supplementary Fig. S3 and Supplementary Text S2). The contact angle between the particle surface and air–water interface on the water side is estimated to be  $\theta_c = 139.5^\circ$  by assuming that the portion submerged in water is a spherical cap (Supplementary Fig. S4).

#### Superdiffusion of single particles on the curved interface

The dynamics of motion of 50 single microgel particles adsorbed onto the air–water interface of the pendant drop and away from the substrate are studied using fluorescence WFM on an instrument equipped with a CCD

camera that records at a speed of  $29 \text{ frames s}^{-1}$  (Scheme 1). The trajectories of three representative microgel particles and the corresponding plots of mean square displacement (MSD)  $\langle r^2(t) \rangle$  vs. elapsed time ( $t_{\text{elapsed}}$ ) are given in Fig. 2a. The MSD plots of particles (i) (Movie S1) and (ii) (Movie S2) exhibit several time segments that are described by a power-law relationship  $\langle r^2(t) \rangle \sim t^\alpha$ , where  $\alpha > 1$ . Superdiffusive behavior therefore occurs. On the other hand, particle (iii) (Movie S3) displays both superdiffusive and subdiffusive ( $\alpha < 1$ ) motions. Its journey from position 1 to 2 is described by  $\alpha = 1.26$  and  $2.15$  (superdiffusion), followed by confined motion between positions 2 and 3. Finally, the particle escapes the confined space and moves superdiffusively to position 4 ( $\alpha = 1.27$  and  $1.56$ ). Clearly, the interfacial environment around the particles is not homogeneous, which gives rise to the observed super/subdiffusive motions. From the MSD analysis of the 50 studied microgel particles, 38 display superdiffusive motion, while the rest exhibit both superdiffusive and confined motion. Figure 2b shows the distribution of 159  $\alpha$  values obtained from the MSD plots of the 50 microgel particles; 87% possess  $\alpha > 1$  (superdiffusion) and 13% possess  $\alpha < 1$  (confined).

The trajectories of 50 microgel particles adsorbed at a *planar* air–water interface (particle density  $\sim 1 \times 10^{-3}$  particles  $\mu\text{m}^{-2}$ ) are also determined. In general, single microgel particles display Brownian motion and move



randomly within an area with a window of  $3.3 \pm 1.3 \mu\text{m}^2$  (5.2 s trajectory) (see Supplementary Fig. S5 for the trajectories of three typical particles at a flat interface and Movie S4). Clearly, their motion is slower than that of microgels attached at a curved interface (Fig. 2). For the latter, the adsorbed particles move superdiffusively within a window with a relatively larger area of  $29.4 \pm 15.4 \mu\text{m}^2$  (5.1 s trajectory) (Fig. 2). The MSD plots of the 3 single particles in Supplementary Fig. S5 are described using  $\langle r^2(t) \rangle = 4Dt$ , where the diffusion coefficients  $D$  for particles 1, 2, and 3 are 0.18, 0.26, and  $0.14 \mu\text{m}^2 \text{s}^{-1}$ , respectively. The average value of  $D$  is  $0.18 \pm 0.08 \mu\text{m}^2 \text{s}^{-1}$  (from 50 particles), which is close to the  $D$  value ( $0.2 \mu\text{m}^2 \text{s}^{-1}$ ) reported for PNIPAM microgels undergoing Brownian motion at a planar air–water interface<sup>47</sup>. Since drift motion is not seen for particles at a planar interface, this suggests that it is also unlikely to attribute to the observed superdiffusion motion for particles adsorbed at the curved interface.

The driving force  $F_s$  that is responsible for the superdiffusive motion is examined using the overdamped Langevin equation for micron-sized particles:  $\gamma v = F_s + F_\eta$ , where  $v$  is the particle velocity,  $\gamma$  is the coefficient of friction and  $F_\eta$  is the random force due to

thermal fluctuations.  $\gamma$  is approximated using Stokes' law:  $\gamma = 6\pi\eta f a_c$ , assuming a sphere of radius  $a_c$ , where  $f$  is the drag coefficient defined by  $f = \frac{1}{2} \left( 1 + \frac{9}{16} \cos\theta_c - 0.139 \cos^2\theta_c \right)$  and  $\eta$  is the viscosity of water<sup>63</sup>. To determine  $F_s$  for each time step  $\Delta t$  of the trajectory, the first-order integrator of the Langevin equation is employed:  $r(t + \Delta t) = r(t) + \frac{F_s}{\gamma} \Delta t + \sqrt{\frac{2k_B T \Delta t}{\gamma}} \xi$ , where  $r(t)$  and  $r(t + \Delta t)$  are the positions of the particle at times  $t$  and  $t + \Delta t$ , respectively, and  $\xi$  is a random number drawn from a standard normal distribution. A total of 5000 independent runs were performed on particles (i) and (ii) in Fig. 2a, and the histograms for  $F_s$  are presented in Fig. 2c. The computed  $F_s$  values range between 1 and 120 fN, with fewer than 1.9% of the  $F_s$  values being less than 1 fN. The average total energy needed to transport the particle from the start to end of its trajectory is  $143.7 k_B T$  and  $149.9 k_B T$  for (i) and (ii), respectively.

### Two-particle cluster formation

The evolution of two-particle cluster formation at a curved interface is studied using WFM tracking of the motion of a pair of microgel particles. Figure 3a–f shows

the trajectories and MSD plots, respectively, for three representative particle pairs before and after cluster formation (Movies S5–S7 for pair (i)–(iii), respectively). For cluster formation to occur, the particle pair needs to come close enough without moving away from each other. There are several ways to do so: in pair (i) (Fig. 3a, d), one of the particles moves subdiffusively in a restricted space (blue trajectory) while the other moves superdiffusively toward its partner (red trajectory); in pair (ii) (Fig. 3b), both particles are first transported superdiffusively from their initial positions (1) to their new positions (2) where the particles then experience confined motion (Fig. 3e) before cluster formation (2 → 3); and in pair (iii) (Fig. 3c, f), both particles move with directed motion to a common space that allows them to combine. The fits to the relationship  $\langle r^2(t) \rangle \sim t^\alpha$  for the various particles are given in Supplementary Fig. S6.

Figure 3g–i shows the interparticle distance  $d$  vs. time plots for the above three particle pairs (i)–(iii), respectively. A salient feature observed is that  $d$  does not decrease continuously. In particular, just before cluster formation, the particles maintain a relatively long-lived ( $t_e > 2$  s) interparticle separation  $d_e$  that only fluctuates slightly; specifically,  $d_e = 4.95 \pm 0.25$ ,  $4.45 \pm 0.35$ , and  $6.02 \pm 0.47 \mu\text{m}$  for pair (i–iii), respectively. During this time, the particle pair achieves a pseudoequilibrium state where the pairwise interaction potential  $U(d_e) = 0$ . Subsequently, the particles approach each other quickly ( $< 40$  time steps) to combine. The interaction potential  $U(d)$  for a particle pair separated by a distance  $d$  ( $< d_e$ ) is thus given by  $U(d) = \int_{d_e}^d F_{\text{int}}(d') dd'$ , where  $F_{\text{int}}(d')$  is the interaction force. Assuming that  $F_\eta$  is significantly weaker than  $F_{\text{int}}(d)$  in the Langevin equation, the latter is expressed as  $F_{\text{int}} = \gamma v(d)$ , where  $v(d)$  is the velocity of the approaching particles along the trajectory joining their centers<sup>33</sup>. Figure 3j shows the plot of  $U(d)$  vs.  $d$  for pair (iii) in Fig. 3c, where  $d_e = 5.82 \mu\text{m}$  is used. Based on the above experimental results, the following questions are asked: why do single microgel particles exhibit superdiffusive and confined behavior, and how are two-particle clusters formed at low particle densities?

### Interface with nonuniform principal curvatures

A colloidal particle trapped at a curved liquid interface with varying curvature experiences a lateral force that pushes it to regions of high deviatoric curvatures<sup>31,32,50–52</sup>. For a particle with a roughened surface and pinned contact line, the difference in curvature capillary energy between two locations is given by:  $\Delta E = -\sigma \pi a^2 \left( \frac{h_p \Delta c}{2} + \frac{3a^2 \Delta H_o^2}{4} \right)$ , where  $\sigma$  is the interfacial tension,  $h_p$  is the amplitude of the quadrupolar mode of the distortion created by the particle, and  $\Delta c$  and  $\Delta H_o$  are the differences in deviatoric and mean curvatures at the two locations, respectively<sup>64</sup>. The  $h_p$

value of the P(NIPAM-co-AEMH) microgel particles is estimated to be  $\sim 10$  nm in air using atomic force microscopy (i.e., surface roughness) (Supplementary Fig. S7) and is assumed to remain invariant in water<sup>65</sup>. In the following sections, we show that the air-water interface of the pendant water droplet has nonuniform principal curvatures and results in a distribution of  $\Delta c$ .

Small sections of the curved surface of the pendant drop are first imaged using a fluorescence confocal microscope with interface-trapped dye-labeled microgel particles acting as fluorescent probes (Supplementary Fig. S8). Adjacent  $x$ – $y$  plane interfaces (arcs) are separated by  $2 \mu\text{m}$  along the vertical  $z$ -axis. Each arc that displays discernible bright spots from microgel particles (density =  $0.08$  particle  $\mu\text{m}^{-1}$ ) is fitted to a cubic polynomial function (Supplementary Fig. S9). A reconstructed interface is then obtained from data points generated from the cubic equations. Supplementary Fig. S10 shows the reconstructed curved interface corresponding to the confocal image in Supplementary Fig. S8.

By considering a parametric curve  $r(x, y, z) = (x, y = a + bx + cx^2 + dx^3, z)^T$ , the first fundamental form coefficients are computed from  $E = \mathbf{r}_x \cdot \mathbf{r}_x$ ,  $F = \mathbf{r}_x \cdot \mathbf{r}_y$  and  $G = \mathbf{r}_y \cdot \mathbf{r}_y$ , where the subscripts  $x$  and  $y$  denote the partial differentiation with respect to  $x$  and  $y$ , respectively<sup>66</sup>. The second fundamental form coefficients are computed from  $L = \mathbf{r}_{xx} \cdot \mathbf{N}$ ,  $M = [(\mathbf{r}_{xy} + \mathbf{r}_{yx})/2] \cdot \mathbf{N}$  and  $N = \mathbf{r}_{yy} \cdot \mathbf{N}$ , where  $\mathbf{N}$  is the unit surface normal vector defined as  $\mathbf{N} = (\mathbf{r}_x \times \mathbf{r}_y) / |\mathbf{r}_x \times \mathbf{r}_y|$ . The Gaussian ( $K$ ) and mean ( $H$ ) curvatures at each point on the interface are obtained from  $K = (LN - M^2)/(EG - F^2)$  and  $H = (EN + GL - 2FM)/2(EG - F^2)$ , where  $E$ ,  $F$ , and  $G$  are the first fundamental form coefficients, and  $L$ ,  $M$ , and  $N$  are the second fundamental form coefficients<sup>66</sup>. The principal curvatures  $\kappa_1$  and  $\kappa_2$  are computed using the relationships  $K = \kappa_1 \kappa_2$  and  $H = (\kappa_1 + \kappa_2)/2$  and the deviatoric curvature from  $c = |\kappa_1 - \kappa_2|$ .

Figure 4a shows the side profile of the pendant drop interface in the  $y$ – $z$  plane for  $x = 229$ ,  $375$ , and  $554 \mu\text{m}$ . The arcs observed in Fig. 4a are uneven and display depressions and bulges. For the arc at  $x = 554 \mu\text{m}$ , the mean curvature at point i is  $1.3 \times 10^{-3} \mu\text{m}^{-1}$  and increases to  $3.4 \times 10^{-3} \mu\text{m}^{-1}$  at point ii due to an elevation of the surface away from the liquid phase. At point iii, an inward depression toward the liquid phase results in  $H = -6.7 \times 10^{-3} \mu\text{m}^{-1}$ . Therefore, the pendant drop exhibits a distribution of curvatures. The Bond number of the microgel particle, calculated from  $B_o = (\Delta \rho g a^2)/\sigma$ , where  $\Delta \rho$  is the density difference between the two phases, is  $\sim 10^{-8} \ll 1$ , indicating negligibly small effects from gravity. The roughness of the reconstructed air-water interface is  $\sim 3.2 \mu\text{m}$  (Text S3), which means that the few nm-scale deformation caused by the trapped microgel particles is not responsible for the nonuniform principal curvatures

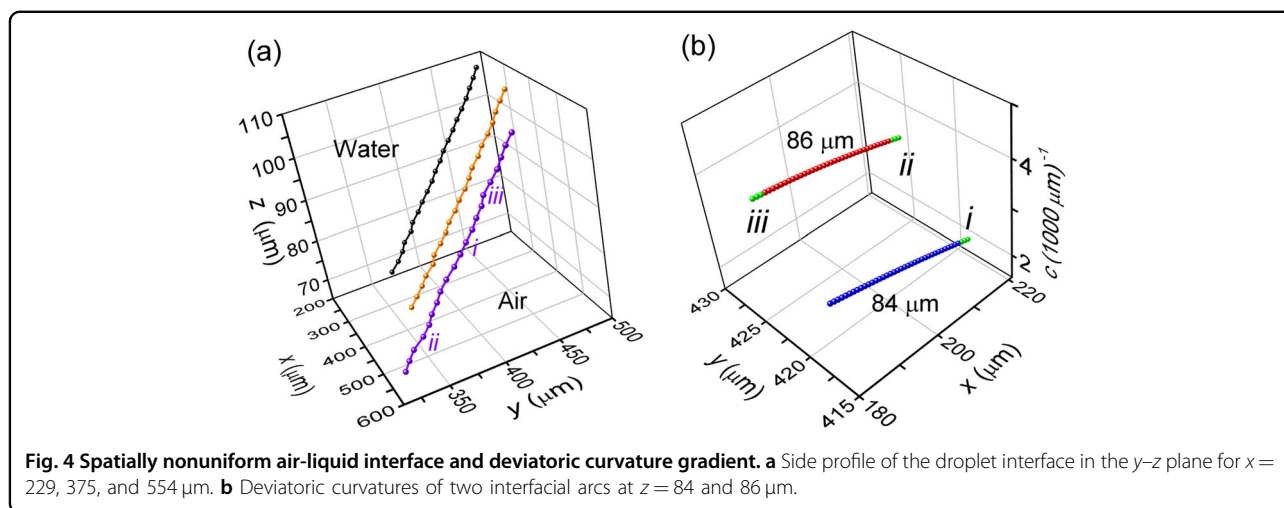


**Fig. 4** Spatially nonuniform air-liquid interface and deviatoric curvature gradient. **a** Side profile of the droplet interface in the  $y$ - $z$  plane for  $x = 229, 375, \text{ and } 554 \mu\text{m}$ . **b** Deviatoric curvatures of two interfacial arcs at  $z = 84 \text{ and } 86 \mu\text{m}$ .

of the former state<sup>34</sup>. On the other hand, when the  $B_o$  value of the pendant drop is  $\sim 1.1$ , gravity deformation of the shape of the droplet away from a perfect hemisphere cannot be ignored<sup>67</sup>. In an ideal case, the shape of the pendant drop is described by the balance between gravity and surface tension:  $\rho gh = 2\sigma H - \left(\frac{2\sigma}{R_o}\right)$ , where  $h$  is the height of the drop from the apex and  $R_o$  is the radius of curvature at the apex. Therefore, the principal radii of curvature vary with  $h$ . In addition, the rough substrate surface may give rise to a heterogeneous distribution of the contact angle, which can cause further deformation to the microscopic environment surrounding the microgel particles.

The superdiffusive behavior of single microgel particles is rationalized by considering a positive  $\Delta c$  ( $+\Delta c$ ) arising from the surface with nonuniform principal curvatures. Given that the depth of view of the fluorescence wide-field microscope is  $\sim 4 \mu\text{m}$ , the trajectory of a microgel particle recorded using WFM may arise from its motion over an area that is approximately between two adjacent reconstructed interfaces (e.g., Fig. 4b). We take a small section of the curved surface between  $z = 84$  and  $86 \mu\text{m}$  as an example, where the interfaces at  $z = 82$  and  $88 \mu\text{m}$  have lower  $c$  values. The deviatoric curvatures at points i–iii in Fig. 4b are  $1.98 \times 10^{-3}$ ,  $3.40 \times 10^{-3}$ , and  $4.38 \times 10^{-3} \mu\text{m}^{-1}$ , respectively. Therefore, a particle initially at point i moves to point ii with a  $+\Delta c$ -induced energy  $\Delta E_{i \rightarrow ii} = -170.7 k_B T$  followed by a smaller energy  $\Delta E_{ii \rightarrow iii} = -121.2 k_B T$  to point iii due to a smaller  $c$  gradient. Clearly,  $\Delta E$  is of a similar order of magnitude as the energy required to drive superdiffusion (Fig. 2c). Even though the reconstructed surface does not provide curvature information for areas not imaged by the confocal microscope (e.g., between adjacent arcs), we propose that the surface of the pendant drop with nonuniform principal curvatures ensures the existence of several  $+\Delta c$  paths that facilitate the particles being able to undergo superdiffusive migration to points

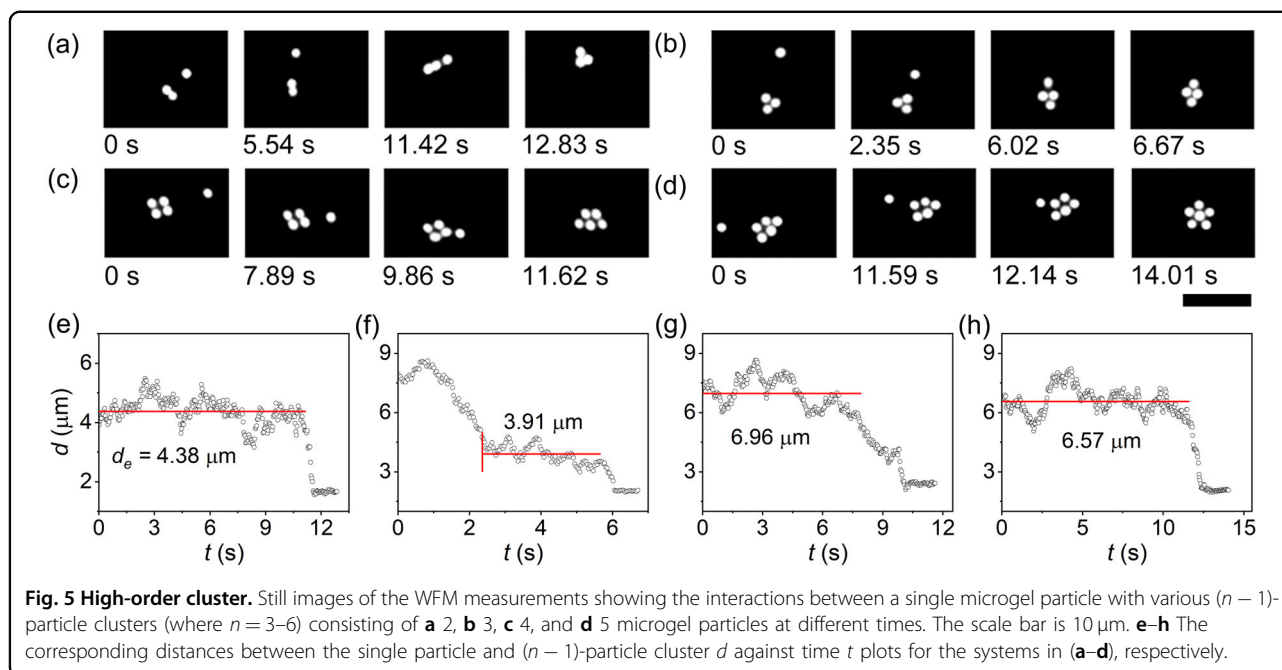
with increased deviatoric curvatures (Fig. 2a). However, once a particle resides in a region with a high deviatoric curvature, it experiences a potential well that confines its motion, especially when there are no surrounding  $+\Delta c$  pathways.

#### Pseudo-equilibrium state during two-particle cluster formation

Cluster formation between two particles initially separated by a distance  $d > 2a$  occurs when they are first transported to a common area with a high deviatoric curvature, as observed in Fig. 3. For  $d < d_e$ , the interaction potential  $U(d) = U_r(d) + U_a(d)$ , where  $U_r(d)$  and  $U_a(d)$  are the pairwise repulsion and attraction potentials at interparticle distance  $d$ , respectively. A pseudoequilibrium state is formed when the particles do not move further or closer to each other (i.e.,  $d = d_e$ ) while maintaining a balance between the attraction and repulsion energies for a period of time (i.e.,  $U_a(d_e) = -U_r(d_e)$ ).

We begin by discussing possible mechanisms that contribute to the repulsion potential for the pseudoequilibrium state. When the microgels are separated by more than a particle distance, electrostatic interaction plays a role, as proposed for long-range ordering of soft particles at interfaces<sup>36,37</sup>. Both the submerged and emergent portions of the particle can contribute. The dipolar repulsion potential is calculated using a standard equation applied to interfacial colloidal particles<sup>20</sup>:  $U_r^{\text{sub}}(d) = Z_{\text{eff}}^2 \frac{\epsilon_a - \epsilon_w}{2\pi\epsilon_0\epsilon_w^2} \frac{\kappa^{-2}}{d^3}$ , where  $\epsilon_a$  and  $\epsilon_w$  are the dielectric constants of air and water, respectively. For ionic microgels, the effective charge  $Z_{\text{eff}}$  is calculated by considering both the bare charge  $Z$  and adsorbed counterions of opposite charge within the submerged portion of the microgels<sup>68,69</sup>:  $Z_{\text{eff}} = f_{\text{sub}} Z \frac{3}{\kappa a_w} \left(1 + \frac{1}{\kappa a_w}\right) e^{-\kappa a_w} \left[\cosh(\kappa a_w) - \frac{\sinh(\kappa a_w)}{\kappa a_w}\right]$ , where  $f_{\text{sub}}$  ( $=0.25$ ) is the fraction submerged. In addition, long-range repulsion between the emergent parts of the microgels is





caused by monopoles that are not neutralized upon surfacing from the water phase and is inversely proportional to  $d$  (i.e.,  $U_r^{em}(d) \propto d^{-1}$ )<sup>22</sup>. Unfortunately, the determination of  $U_r^{em}(d)$  is nontrivial since the fraction of monopoles is unknown. Steric repulsion is not considered at this juncture because the coronas of the microgels are unlikely to be in contact.

Since soft particles have rough and chemically heterogeneous surfaces<sup>16</sup> and the deformed interface of microgel particles deviates from a circular shape (Fig. 1), higher multipole modes may play a role. Apart from the capillary force, the curvature capillary energy for a microgel particle at a curved interface gives rise to a local curvature capillary torque ( $T_{\text{curv}}$ ) that aligns the quadrupolar mode along its first principal axis<sup>70</sup>. Due to the slight irregular shape of a particle and the presence of nonuniform principal curvatures, the orientations of the approaching microgels are fixed by  $T_{\text{curv}}$ , which may facilitate higher multipole order repulsion (e.g., quadrupole–hexapole)<sup>43</sup>. Therefore, capillary repulsion can contribute to  $U_r(d)$ . Further studies that should shed light on this mechanism, include (i) understanding the contribution from higher multipole orders, (ii) determining the transition interparticle distance between far-field and near-field interactions, and (iii) obtaining analytical expressions to quantify interaction potentials between trapped particles at a curved interface<sup>32</sup>.

Interestingly, apart from long-range capillary attraction<sup>47</sup>, the so-called attraction potential arising when particles attempt to approach each other during their motion to an area with high curvature must also be considered. It is worth noting that short-range van der Waals attractions are not

important at the pseudoequilibrium separation  $d_e$ . Therefore, prior to two-particle cluster formation, the balance between various possible potentials (e.g., pairwise electrostatic interaction and repulsion from higher multipole orders,  $+\Delta c$ -induced energy pushing the pair of particles to high curvature and interparticle capillary attraction) creates a pseudoequilibrium state where the interparticle distance remains relatively invariant for a long period of time. Since  $U(d_e) = 0$ , the *minimum* value of  $U_a(d_e)$  for pair (iii) in Fig. 3 is estimated from  $U_r^{\text{sub}}(d_e) \sim 0.9 k_B T$ , bearing in mind that monopole–monopole interactions between the large emergent parts and higher multipole mode capillary repulsion further increase the repulsion potential.

After a time period  $t_e$ , the particles move quickly toward each other and combine. Since  $d_e > 2a$ , a strong pairwise attraction must be in operation to allow the particles to form clusters. Long-range electrostatic interaction plays only a minor role when the particles approach close enough so that their coronas begin to be in contact, and steric interaction involving cross-linked chains at the particle peripherals becomes important<sup>38–42</sup>. It must be stressed that further experimental and theoretical investigations are needed to fully elucidate the exact nature of the long-range attraction potential needed for particles in the pseudoequilibrium state to quickly approach each other to form clusters.

#### Pseudoequilibrium state in higher-order cluster formation

The formation of a pseudoequilibrium state is also observed prior to the formation of higher-order particle ( $n > 2$ ) clusters. As shown by the still WFM images at

various times and the corresponding  $d$  vs.  $t$  plots (Fig. 5), the distance between an incoming particle and a  $(n - 1)$ -particle cluster (where  $n = 3-6$ ) ( $d$ ) remains relatively invariant before the particle undergoes combination to form an  $n$ -particle cluster (see Movie S8 for the evolution of a six-particle cluster). In this case, the balance of the single particle/ $(n - 1)$ -particle cluster repulsion and attraction (e.g.,  $+\Delta c$ -induced energies and capillary attraction) acting on the moieties leads to the observed pseudoequilibrium state.

## Conclusion

In summary, single ionic microgel particles adsorbed onto an air–water interface with nonuniform principal curvatures experience capillary forces that are responsible for their superdiffusive motion. These forces are also important for transporting a pair of particles that are initially far apart to a common area on the interface with a high deviatoric curvature. The balance between pairwise repulsion energy, capillary attraction energy, and energy that arises when the particles attempt to approach each other while moving to a common high curvature space allows the particles to maintain a relatively fixed interparticle distance for a period of time before a long-range attraction potential is activated. In addition, we have provided an alternative explanation for the evolution of (two-particle) cluster formation involving a yet reported pseudoequilibrium state. The above observation is also noted for higher-order particle clusters.

## Acknowledgements

W. Bi acknowledges the financial support from the Heilongjiang Provincial Natural Science Foundation of China (LH2019B004). E.K.L. Yeow acknowledges the Singapore Ministry of Education MoE Tier 1 fund (RG6/18) for financial support.

## Conflict of interest

The authors declare that they have no conflict of interest.

## Publisher's note

Springer Nature remains neutral with regard to jurisdictional claims in published maps and institutional affiliations.

**Supplementary information** is available for this paper at <https://doi.org/10.1038/s41427-020-00254-z>.

Received: 31 March 2020 Revised: 7 September 2020 Accepted: 17 September 2020

Published online: 6 November 2020

## References

- Ballard, N., Law, A. D. & Bon, S. A. F. Colloidal particles at fluid interfaces: behavior of isolated particles. *Soft Matter* **15**, 1186–1899 (2019).
- Li, Z., Geisel, K., Richtering, W. & Ngai, T. Poly(N-isopropylacrylamide) microgels at the oil–water interface: adsorption kinetics. *Soft Matter* **9**, 9939–9946 (2013).
- Pinaud, F. et al. Adsorption of microgels at an oil–water interface: correlation between packing and 2D elasticity. *Soft Matter* **10**, 6963–6974 (2014).
- Deshmukh, O. S. et al. Equation of state and adsorption dynamics of soft microgel particles at an air–water interface. *Soft Matter* **10**, 7045–7050 (2014).
- Style, R. W., Isa, L. & Dufresne, E. R. Adsorption of soft particles at fluid interfaces. *Soft Matter* **11**, 7412–7419 (2015).
- Destribats, M. et al. Soft microgels as pickering emulsion stabilisers: role of particle deformability. *Soft Matter* **7**, 7689–7698 (2011).
- Richtering, W. Responsive emulsions stabilized by stimuli-sensitive microgels: emulsions with special non-pickering properties. *Langmuir* **28**, 17218–17229 (2012).
- Zielińska, K., Sun, H., Campbell, R. A., Zorbakhsh, A. & Resmini, M. Smart nanogels at the air/water interface: structural studies by neutron reflectivity. *Nanoscale* **8**, 4951–4960 (2016).
- Minato, H. et al. The deformation of hydrogel microspheres at the air/water interface. *Chem. Commun.* **54**, 932–935 (2018).
- Brijitta, J. & Schurtenberger, P. Responsive hydrogel colloids: structure, interactions, phase behavior, and equilibrium and nonequilibrium transitions of microgel dispersions. *Curr. Opin. Colloid Interface Sci.* **40**, 87–103 (2019).
- Del Monte, G. et al. Numerical insights on microgels: structure and swelling behaviour. *Soft Matter* **15**, 8113–8128 (2019).
- Rovigatti, L., Gnan, N., Tavagnacco, L., Moreno, A. J. & Zaccarelli, E. Numerical modelling of non-ionic microgels: an overview. *Soft Matter* **15**, 1108–1119 (2019).
- Geisel, K., Isa, L. & Richtering, W. Unravelling the 3D localization and deformation of responsive microgels at oil/water interfaces: a step forward in understanding soft emulsion stabilizers. *Langmuir* **28**, 15770–15776 (2012).
- Richtering, W. Responsive emulsions stabilized by stimuli-sensitive microgels: emulsions with special non-pickering properties. *Langmuir* **2012**, 17218–17229 (2012).
- Rey, M., Fernandez-Rodriguez, M. A., Karg, M., Isa, L. & Vogel, N. Poly-N-isopropylacrylamide nanogels and microgels at fluid interfaces. *Acc. Chem. Res.* **53**, 414–424 (2020).
- Deshmukh, O. S., Ende, D., van der Stuart, M. C., Mugele, F. & Duits, M. H. G. Hard and soft colloids at fluid interfaces: adsorption, interactions, assembly & rheology. *Adv. Colloid Interface Sci.* **222**, 215–227 (2015).
- Camerin, F. et al. Microgels adsorbed at liquid-liquid interfaces: a joint numerical and experimental study. *ACS Nano* **13**, 4548–4559 (2019).
- Arismendi-Arrieta, D. J. & Moreno, A. J. Deformability and solvent penetration in soft nanoparticles at liquid-liquid interface. *J. Colloid Interface Sci.* **570**, 212–223 (2020).
- Pieranski, P. Two-dimensional interfacial colloidal crystals. *Phys. Rev. Lett.* **45**, 569–572 (1980).
- Hurd, A. J. The electrostatic interaction between interfacial colloidal particles. *J. Phys. A* **18**, L1055–L1060 (1985).
- Robinson, D. J. & Earnshaw, J. C. Earnshaw, Initiation of aggregation in colloidal particle monolayers. *Langmuir* **9**, 1436–1438 (1993).
- Moncho-Jordá, A., Martínez-López, F., González, A. E. & Hidalgo-Álvarez, R. Role of long-range repulsive interactions in two-dimensional colloidal aggregation: experiments and simulations. *Langmuir* **18**, 9183–9191 (2002).
- Wickman, H. H. & Korley, J. N. Colloid crystal self-organization and dynamics at the air/water interface. *Nature* **393**, 445–447 (1998).
- Stamou, D., Duschl, C. & Johannsmann, D. Long-range attraction between colloidal spheres at the air–water interface: the consequence of an irregular meniscus. *Phys. Rev. E* **62**, 5263–5272 (2000).
- Oettel, M. & Dietrich, S. Colloidal interactions at fluid interface. *Langmuir* **24**, 1425–1441 (2008).
- McGorty, R., Fung, J., Kaz, D. & Manoharan, V. N. Colloidal self-assembly at an interface. *Mater. Today* **13**, 34–42 (2010).
- Nikolaides, M. G. et al. Electric-field-induced capillary attraction between like-charged particles at liquid interface. *Nature* **420**, 299–301 (2002).
- Megens, M. & Aizenberg, J. Like-charged particles at liquid interfaces. *Nature* **424**, 1014 (2003).
- Chen, W., Tan, S., Ng, T. –K, Ford, W. T. & Tong, P. Long-ranged attraction between charged polystyrene spheres at aqueous interfaces. *Phys. Rev. Lett.* **95**, 218301 (2005).
- Dominguez, A., Frydel, D. & Oettel, M. Multipole expansion of the electrostatic interaction between charged colloids at interfaces. *Phys. Rev. E* **77**, 020401(R) (2008).
- Würger, A. Curvature-induced capillary interaction of spherical particles at a liquid interface. *Phys. Rev. E* **74**, 041402 (2006).
- Léandri, J. & Würger, A. Trapping energy of a spherical particle on a curved liquid interface. *J. Colloid Interface Sci.* **405**, 249–255 (2013).

33. Loudet, J. C., Alsayed, A. M., Zhang, J. & Yodh, A. G. Capillary interactions between anisotropic colloidal particles. *Phys. Rev. Lett.* **94**, 018301 (2005).
34. Ershov, D., Sprakel, J., Appel, J., Stuart, M. A. C. & van der Gucht, J. Capillarity-induced ordering of spherical colloids on an interface with anisotropic curvature. *Proc. Natl Acad. Sci. USA* **110**, 9220–9224 (2013).
35. Bergman, M. J. et al. A new look at effective interactions between microgel particles. *Nat. Commun.* **9**, 5039 (2018).
36. El-Tawary, A. S. et al. Multiple structural transitions in Langmuir monolayers of charged soft-shell nanoparticles. *Langmuir* **34**, 3909–3917 (2018).
37. Gavrilov, A. A., Richtering, W. & Potemkin, I. I. Polyelectrolyte microgels at a liquid-liquid interface: swelling and long-range ordering. *J. Phys. Chem. B* **123**, 8590–8598 (2019).
38. Geisel, K., Isa, L. & Richtering, W. The compressibility of pH-sensitive microgels at the oil–water interface: higher charge leads to less repulsion. *Angew. Chem. Int. Ed.* **53**, 4905–4909 (2014).
39. Geisel, K., Richtering, W. & Isa, L. Highly ordered 2D microgel arrays: compression versus self-assembly. *Soft Matter* **10**, 7968–7976 (2014).
40. Picard, C. et al. Organization of microgels at the air-water interface under compression: role of electrostatics and cross-linking density. *Langmuir* **33**, 7968–7981 (2017).
41. Scheidegger, L. et al. Compression and deposition of microgel monolayers from fluid interfaces: particle size effects on interface microstructure and nanolithography. *Phys. Chem. Chem. Phys.* **19**, 8671–8680 (2017).
42. Rey, M., Hou, X., Tang, J. S. J. & Vogel, N. Interfacial arrangement and phase transitions of PNIPAm microgels with different crosslinking densities. *Soft Matter* **13**, 8717–8727 (2017).
43. Danov, K. D., Kralchevsky, P. A., Naydenov, B. N. & Brenn, G. Interactions between particles with an undulated contact line at a fluid interface: capillary multipoles of arbitrary order. *J. Colloid Interface Sci.* **287**, 121–134 (2005).
44. Danov, K. D. & Kralchevsky, P. A. Capillary forces between particles at a liquid interface: general theoretical approach and interaction between capillary multipoles. *J. Colloid Interface Sci.* **154**, 91–103 (2010).
45. Yao, L. et al. Near field capillary repulsion. *Soft Matter* **9**, 779–786 (2013).
46. Sharifi-Mood, N., Liu, I. B. & Stebe, K. J. in *Soft Matter Self-Assembly* (eds Likos, C. N., Sciortino, F., Zaccarelli, E. & Zihler, P.) 165–216 (IOS, Amsterdam, SIF, Bologna, 2016).
47. Cohin, Y. et al. Tracking the interfacial dynamics of PNIPAM soft microgel particles adsorbed at the air-water interface and in thin liquid films. *Rheol. Acta* **52**, 445–454 (2013).
48. Huang, S., Gawlitza, K., von Klitzing, R., Steffen, W. & Auernhammer, G. Structure and rheology of microgel monolayers at the water/oil interface. *Macromolecules* **50**, 3680–3689 (2017).
49. Huang, S. et al. Microgels at the water/oil interface: in situ observation of structural aging and two-dimensional magnetic bead microrheology. *Langmuir* **32**, 712–722 (2016).
50. Cavallaro, M. Jr., Botto, L., Lewandowski, E. P., Wang, M. & Stebe, K. J. Curvature-driven capillary migration and assembly of rod-like particles. *Proc. Natl Acad. Sci. USA* **108**, 20923–20928 (2011).
51. Blanc, C. et al. Capillary force on a micrometric sphere trapped at a fluid interface exhibiting arbitrary curvature gradients. *Phys. Rev. Lett.* **111**, 058302 (2013).
52. Li, N. et al. Curvature-driven migration of colloids on tense bilayers. *Langmuir* **33**, 600–610 (2017).
53. Sarfati, R. & Dufresne, E. R. Long-range attraction of particles adhered to lipid vesicles. *Phys. Rev. E* **94**, 012604 (2016).
54. Bi, W., Teguh, J. S. & Yeow, E. K. L. Visualizing polymer crystallization in ultrathin layers using a single-macromolecule tracking method. *Phys. Rev. Lett.* **102**, 048302 (2009).
55. Lu, S. et al. Loss of collective motion in swarming bacteria undergoing stress. *Phys. Rev. Lett.* **111**, 208101 (2013).
56. Ow, M. J. K., Ng, J. J., Quek, B. Y. L., Yeow, E. K. L. & Zhang, Z. Super-resolution fluorescence microscopy reveals nanoscale catalytic heterogeneity on single copper nanowire. *ACS Appl. Nano Mater.* **3**, 3163–3167 (2020).
57. Bi, W. & Yeow, E. K. L. Domain coalescence-induced nucleation and anomalous growth of holes in thin polymer blend film. *Phys. Rev. Lett.* **106**, 078001 (2011).
58. Bi, W., Wu, X. & Yeow, E. K. L. Unconventional multiple ring structure formation from evaporation-induced self-assembly of polymers. *Langmuir* **28**, 11056–11063 (2012).
59. Lu, S. et al. Lipopolysaccharide-affinity copolymer senses the rapid motility of swarmer bacteria to trigger antimicrobial drug release. *Nat. Commun.* **9**, 4277 (2018).
60. Alsayed, A. M., Islam, M. F., Zhang, J., Collings, P. J. & Yodh, A. G. Premelting at defects within bulk colloidal crystals. *Science* **309**, 1207–1210 (2005).
61. Ngo, T. T. A simple photometric determination of solid supported amino groups. *J. Biochem. Biophys. Methods* **12**, 349–354 (1986).
62. Sbalzarini, I. F. & Koumoutsakos, P. Feature point tracking and trajectory analysis for video imaging in cell biology. *J. Struct. Biol.* **151**, 182–195 (2005).
63. Dörr, A., Hardt, S., Masoud, H. & Stone, H. A. Drag and diffusion coefficients of a spherical particle attached to a fluid-fluid interface. *J. Fluid Mech.* **790**, 607–618 (2016).
64. Sharifi, N., Liu, I. B. & Stebe, K. J. Curvature capillary migration of microspheres. *Soft Matter* **11**, 6767–6779 (2015).
65. Li, M., Bresson, B., Cousin, F., Fretigny, C. & Tran, Y. Submicrometric films of surface-attached polymer network with temperature-responsive properties. *Langmuir* **31**, 11516–11524 (2015).
66. Pressley, A. *Elementary Differential Geometry*. (Springer-Verlag, London, 2010).
67. Mondal, R., Semwal, S., Kumar, P. L., Thampi, S. P. & Basavaraj, M. G. Patterns in drying drops dictated by curvature-driven particle transport. *Langmuir* **34**, 11473–11483 (2018).
68. Denton, A. R. Counterion penetration and effective electrostatic interactions in solutions of polyelectrolyte stars and microgels. *Phys. Rev. E* **67**, 011804 (2003).
69. Riest, J., Mohanty, P., Schurtenberger, P. & Likos, C. N. Coarse-graining of ionic microgels: theory and experiment. *Z. Phys. Chem.* **226**, 711–735 (2012).
70. Lewandowski, E. P., Bernate, J. A., Searson, P. C. & Stebe, K. J. Rotation and alignment of anisotropic particles on nonplanar interfaces. *Langmuir* **24**, 9302–9307 (2008).